

## Advances in wide bandgap SiC for optoelectronics

Haiyan Ou<sup>1,a</sup>, Yiyu Ou<sup>1,b</sup>, Aikaterini Argyraki<sup>1</sup>, Saskia Schimmel<sup>2</sup>, Michl Kaiser<sup>2</sup>, Peter Wellmann<sup>2</sup>, Margareta K. Linnarsson<sup>3</sup>, Valdas Jokubavicius<sup>4</sup>, Jianwu Sun<sup>4,c</sup>, Rickard Liljedahl<sup>4</sup>, and Mikael Syväjärvi<sup>4</sup>

<sup>1</sup> Department of Photonics Engineering, Technical University of Denmark, 2800 Lyngby, Denmark

<sup>2</sup> Materials of Electronics Energy Technology, University of Erlangen-Nuremberg, 91058 Erlangen, Germany

<sup>3</sup> School of Information and Communication Technology, KTH Royal Institute of Technology, 16440 Kista, Sweden

<sup>4</sup> Department of Physics, Chemistry and Biology, Linköping University, 58183 Linköping, Sweden

Received 23 December 2013 / Received in final form 21 January 2014

Published online 10 March 2014 – © EDP Sciences, Società Italiana di Fisica, Springer-Verlag 2014

**Abstract.** Silicon carbide (SiC) has played a key role in power electronics thanks to its unique physical properties like wide bandgap, high breakdown field, etc. During the past decade, SiC is also becoming more and more active in optoelectronics thanks to the progress in materials growth and nanofabrication. This paper will review the advances in fluorescent SiC for white light-emitting diodes, covering the polycrystalline doped SiC source material growth, single crystalline epitaxy growth of fluorescent SiC, and nanofabrication of SiC to enhance the extraction efficiency for fluorescent SiC based white LEDs.

### 1 Introduction

Silicon carbide (SiC) is the only group IV compound semiconductor, and it has more than 200 polytypes. Among them the most commonly used are 4H, 6H, 3C and 15R. The wide bandgap makes SiC a very attractive semiconductor to make devices for applications in high power, high frequency and high temperature environment.

In addition to the traditional applications, SiC has been emerging as a promising material for light-emitting diodes (LED) since Satoshi Kamiyama in 2006 found that nitrogen (N) and boron (B) co-doped SiC has very high donor-acceptor pair (DAP) emission efficiency [1].

The LED light sources are deemed to be the future market leader thanks to their energy saving and long lifetime, compared to conventional incandescent lamps and fluorescent tubes. Currently, most white LED light sources available in the market are made by mixture of blue color from a blue GaN LED and yellow color emitted from the phosphor excited by the blue LED, as shown in Figure 1a. However, there is always a tradeoff between high lumen efficiency and high color rendering index (CRI) for this type of light source. The phosphor degrades much faster than the blue LED chip, so the white light turns blue over time. Moreover, phosphor contains rare earth elements, which could be a price bottleneck considering the huge market in future. In order to overcome these limitations and explore the full potential of the white LED light sources, a

new type white LED light source based on fluorescent SiC (f-SiC), shown in Figure 1b, has been proposed. Compared to the phosphor based white LED light source, this f-SiC based white light source has a number of advantages: (i) it can have both high efficiency and high color rendering index, opposite to the trade-off observed for phosphor based white LED light sources; (ii) it has even longer lifetime due to the monolithic semiconductor structure; (iii) it has simpler thermal management because SiC is a very good thermal conductor; and (iv) it does not contain rare-earth elements.

As shown in Figure 1b, the f-SiC based white LED light source uses f-SiC as a substrate, as well as a wavelength converter. It consists of one layer of 200  $\mu\text{m}$  thick N and B co-doped SiC and one layer of 50  $\mu\text{m}$  thick N and aluminium (Al) co-doped SiC. A near ultraviolet (NUV) diode is grown on top of the N and Al co-doped SiC. A mirror is formed on top of the NUV diode and diverts all the light to exit from the f-SiC substrate. Silicon carbide has a refractive index of 2.65 at 590 nm [2], causing most of the emitted light from f-SiC to be totally reflected into the device. In order to enhance the light extraction efficiency, as shown in Figure 1b, moth-eye nanostructures are implemented at the exit surface of the f-SiC to increase the emission efficiency in the whole visible spectral range.

The operational mechanism of the f-SiC based white LED is illustrated in Figure 2.

The high energy NUV photons emitted from the NUV LED excite electrons from the top of the valence band to the bottom of the conduction band. The free electrons in the conduction band and the free holes left in the valence band will occupy the donor level (N) and acceptor levels (Al and B), respectively, obeying the Fermi-Dirac

<sup>a</sup> e-mail: haou@fotonik.dtu.dk

<sup>b</sup> Present address: Light extraction ApS, Diplomvej 373, 2800 Lyngby, Denmark

<sup>c</sup> Present address: IMEC, Kapeldreef 75, 3001 Leuven, Belgium

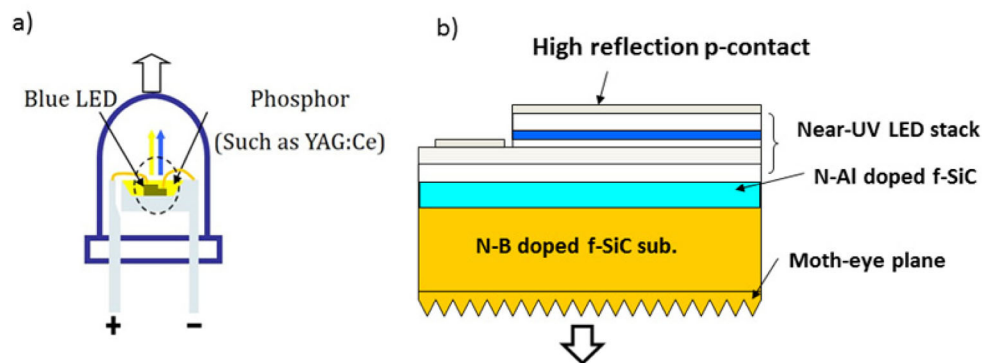


**Fig. 1.** Schematic drawing of (a) traditional phosphor based white LEDs. The white color is mixed with blue color from a LED chip and yellow color from the phosphor excited by the blue and (b) the new fluorescent SiC based white LED.

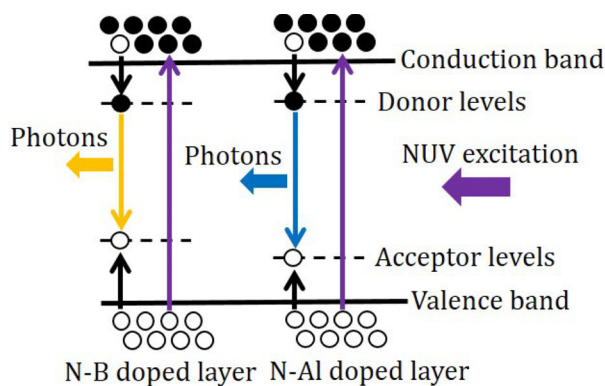


**Fig. 2.** 2 Schematic drawing of the operational mechanism of the f-SiC based white LED light source.

distribution. Then, the electrons on the donor level will recombine with the holes on the acceptor level and emit a low energy photon. The N and Al donor-acceptor-pair (DAP) recombination emits blue light with peak wavelength around 480 nm and N and B DAP emits yellow light with peak wavelength around 590 nm since B is a much deeper acceptor in SiC with respect to the Al. The mixture of the broadband blue light and broadband yellow light makes white light with high CRI.

The f-SiC based white LED light source is an innovative achievement for SiC in optoelectronic devices. In order to accomplish such a new device concept, the development of the material is crucial. In this paper, poly-crystalline f-SiC source material is firstly optimized to grow by physical vapor transport (PVT) after comparing sintering, chemical vapor deposition (CVD) and PVT methods, described in Section 2. Then the source material (poly-crystalline SiC) is used for the growth of high quality single crystalline SiC by fast sublimation growth process (FSGP), described in Section 3. Section 4 presents the optical characterization of the grown epilayers in terms of photoluminescence and Raman spectroscopy to feedback the optimal growth conditions. In order to enhance the extraction efficiency, a couple of different nanostructuring methods were applied on the f-SiC surface and described

in Section 5. Both periodic and non-periodic structures have been demonstrated and effectively increased the emission efficiency. Section 6 summarizes the advances of f-SiC in LED application and gives future perspectives in optoelectronic applications.

## 2 Poly-crystalline fluorescent SiC growth

For the epitaxial growth of high quality fluorescent SiC layers by the FSGP process, the application of a proper solid SiC source material is crucial. In principle, three approaches have been followed so far to produce the desired source material: (a) sintering of SiC powder, (b) chemical vapor deposition (CVD) of microcrystalline SiC and (c) bulk growth of poly-crystalline SiC boules by the physical vapor transport technique. Application of sintered SiC ceramic as source (Fig. 3a) does not lead to mirror like epitaxial layers. In addition, inclusions of secondary phases, most likely carbon related defects, are found in the grown epitaxial SiC material. This type of sintered source easily graphitizes during the SiC epitaxy. In the case of the CVD SiC source material (Fig. 3b) inclusions of 3C-SiC in the 6H-SiC epitaxial layers are found, which are related to the source material used in the epitaxial growth process. A main challenge with this source is the uniform doping introduction. Due to the small size of the inclusions it is concluded that they originate from mass transport between source and seed. Finally, in the case of the PVT growth SiC source (Fig. 3c) the lowest defect density and, hence, best f-SiC layer properties with basically no inclusions are found. In the following this vapor grown source material will be reviewed in detail.

### 2.1 PVT growth process, doping of poly-SiC and wafering process

#### 2.1.1 Growth process principle

Growth of poly-SiC source material is carried out by the state-of-the-art physical vapor transport method (see Fig. 4a). SiC powder is placed at the bottom of the

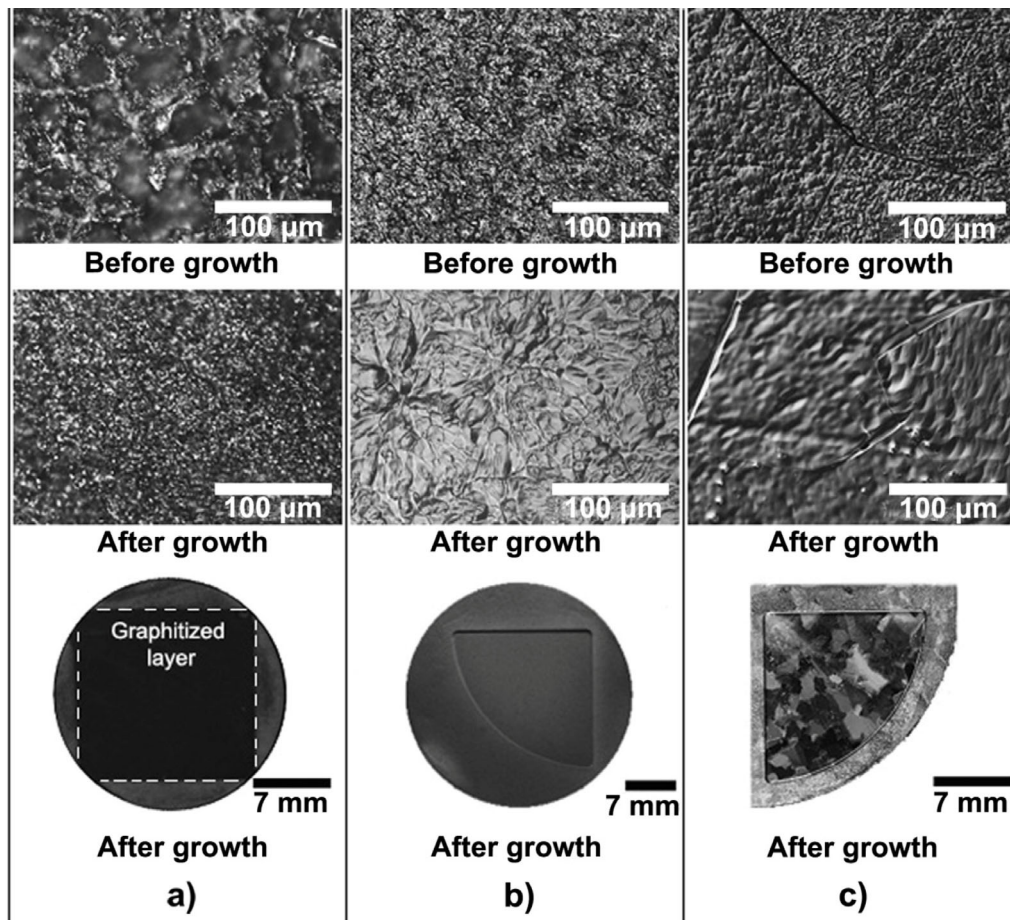


**Fig. 3.** Comparison of three SiC source materials for application during FSGP: (a) sintered poly-crystalline SiC ceramics, (b) CVD grown micro-crystalline SiC source and (c) PVT grown poly-crystalline SiC material. The best layer properties are found in the case of the PVT grown source materials (figure from Ref. [3]).

graphite crucible. As self-seeding substrate a graphite plate is used which is attached to the top of the crucible. Induction heating is performed in a way that a temperature difference of approximately 50 °C is established between the top of the SiC powder source and the poly-SiC growth interface. Typical growth rates lie in the range of 200  $\mu\text{m}/\text{h}$  and 1000  $\mu\text{m}/\text{h}$  and depend on the absolute temperature between 2010 °C and 2300 °C at the crucible top, as well as on the ambient noble gas pressure between 10 mbar and 40 mbar.

### 2.1.2 Doping of SiC by N, B and Al

As dopants nitrogen from the 5th main group was used as donor, while aluminum and boron from the 3rd main group act as acceptors in SiC. The supply of nitrogen can be applied by addition of a  $\text{N}_2$  gas stream to the ambient inert gas stream (Fig. 4a). Due to the chemical inertness of nitrogen and carbon, the dopant gas diffuses through the partially porous graphite parts of the crucible and the surrounding isolation. In the case of the acceptor dopants aluminum and boron the latter procedure fails. Boron may be supplied by addition of boron, in particular

boron carbide ( $\text{B}_4\text{C}$ ) to the source material (Fig. 4b). The dopant transfer from source to growing crystal, as well as incorporation into SiC can be well controlled by the  $\text{B}_4\text{C}$  mass fraction directly added to the SiC source material [4]. In the case of aluminum, however, the dopant supply is more complex. In this case, a too high initial aluminum partial pressure is observed if the dopant is directly added to the SiC source material. In order to suppress the large axial dopant concentration variation in the final SiC crystal, a slightly varied technique, the so-called Modified-PVT (M-PVT) method, is applied [5,6] (Fig. 4c). In the M-PVT setup an aluminum source ( $\text{Al}_4\text{C}_3$ ) is placed at a lower temperature and, hence, smaller aluminum vapor pressure in the near vicinity of the PVT crucible. Via a feeding gas pipe the dopant is continuously added to the growth chamber exhibiting a constant dopant flow during the growth process.

### 2.1.3 Wafering

Subsequent to growth the poly-SiC boules are grinded down to a proper diameter of typically 50 mm. Wafering is carried out by a diamond inside hole saw. Wafer

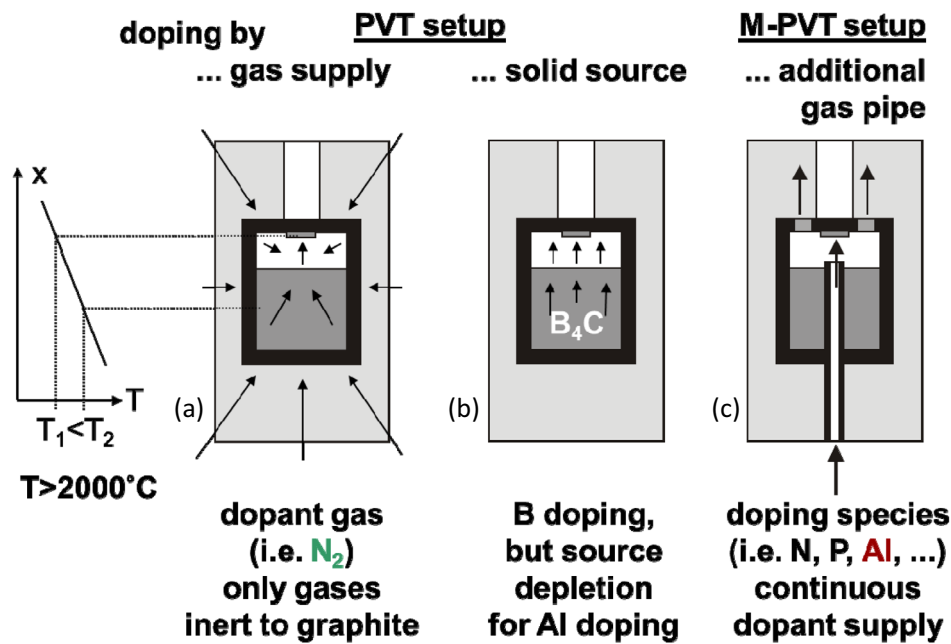


Fig. 4. Sketch of the PVT growth reactor interior for the preparation of doped poly-SiC boules.

thickness lies between  $500\ \mu\text{m}$  and  $1\ \text{mm}$ . For the application as source material during FSGP a removal of the sawing damage by a lapping or rough polishing step is necessary.

## 2.2 Structural properties of poly-SiC wafers

During poly-crystalline growth of SiC a pronounced grain growth is observed which is attributed to a strong grain selection process [7]. Figure 5 shows optical scanning images of three poly-SiC wafers from the same boule directly (a) after nucleation, (b) after 10 h and (c) after 20 h of growth time. A statically pressed highly purified graphite was used as substrate plate. The polytypes differ from 4H-SiC, 6H-SiC and 15R-SiC. No 3C-SiC was found which may be related to the high growth temperature above  $2100\ ^\circ\text{C}$ . Although no precise and well defined grain orientation is observed by X-ray Laue pattern analysis (40 kV, 30 mA, 5 min), most grains exhibit a trend towards (0001) orientation with inclination variation between  $0^\circ$  and  $30^\circ$ . Between the grains no obvious preferential alignment, i.e. formation of particular grain boundaries, was detected so far. Noteworthy is that 15R-SiC grains usually exhibit off orientation towards (0001) of more than  $15^\circ$ . From KOH defect etching analysis it is concluded that more than 90% of the larger grains (Figs. 5b and 5c) show C-face polarity. Pretreatment of the statically pressed graphite nucleation plate surface by coating with pyrolytic graphite showed an impact on the variation of grain orientation and grain selection process. Compared to the partially porous isotatic pressed graphite with mainly random grain orientation, the pyrolytic coating exhibits no open porosity and a [001]-texture and slightly reduced surface roughness. As main result, a SiC grain size in the 10 mm range has been

observed, but further studies are necessary to quantify these new findings (Fig. 6) [8]. The weak impact of the SiC grain polytype and orientation on the growth rate during FSGP will be discussed in Section 2.4.

## 2.3 Electrical properties of poly-SiC wafers

The N, B and Al doping concentration of the poly-SiC source is set by (i) the amount of dopant supply, (ii) growth rate and (iii) growth kinetic related boundary conditions (e.g. C/Si ratio of the SiC vapor) which are related to the growth parameters like temperature field and inert gas pressure. Amount of dopant supply is mainly given by intentional feeding; however, residual doping of the powder SiC source prior PVT growth and contamination from the crucible material also has to be considered. In the case of B doping with target values in the mid  $10^{18}\ \text{cm}^{-3}$  (chemical concentration) the amount of addition to the SiC source powder is the dominant factor.

Figure 7 shows the experimental evaluation between addition of boron as  $\text{B}_4\text{C}$  to the SiC powder source and chemical composition inside the poly-SiC crystal for a number of wafers. The dopant transfer from source to seed crystal is well defined by the amount of supply and growth parameters (temperature and pressure). Doping variations of ca. 25% to 50% are mainly related to kinetic dopant incorporation effects due to varying crystallographic orientations of the grains in the range of tilt angles around between  $0^\circ$  and  $30^\circ$  towards (0001) orientation (see Sect. 2.2). While local doping may vary around the mentioned 25 to 50%, the medium values can be set around 10% to 15% by proper and reproducible setting of the growth process parameters.

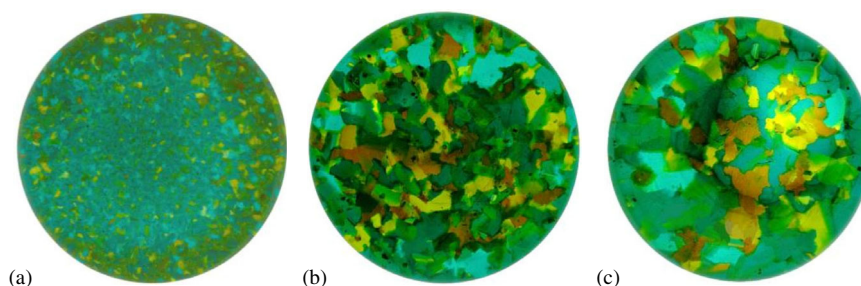


**Fig. 5.** White light absorption scans of a series of three 50 mm poly-SiC wafers from boule: (a) directly after nucleation, (b) after 10 h and (c) after 20 h of growth time (figure from Ref. [7]).

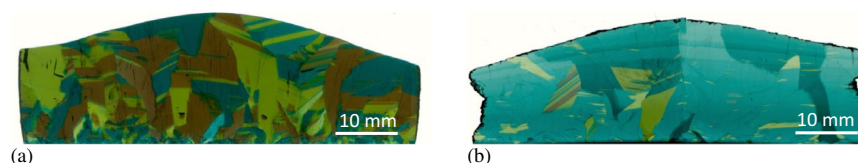


**Fig. 6.** Cross section of two poly-SiC crystals grown on isostatic graphite at 2250 °C (a) and on pyrolytic graphite at 2350 °C (b). The diameter of the cross section of the boules of >60 mm is shown before grinding down to the standard size of 50 mm (figure from Ref. [8]).

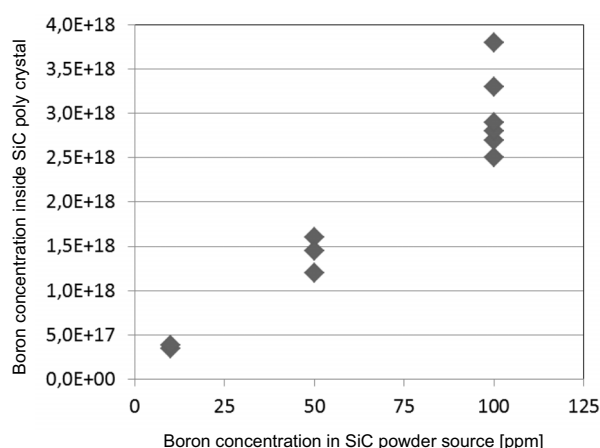


**Fig. 7.** Plot of boron incorporation into poly-SiC during PVT growth.

## 2.4 Impact of structural source properties on growth rate during FSGP

In order to study the impact of the structural properties of the poly-SiC source wafers on the FSGP growth rate, special experiments with masking techniques were carried out. During FSGP a graphite mask was placed between source and seed to select certain SiC grains from the source material and to follow the impact of polytype and grain orientation on the epitaxial layer thickness, as shown in Figure 8.

The graphical analysis of the limited data exhibits a clear correlation between off-axis orientation (tilt of the grain off orientation towards (0001)) and epitaxial layer thickness. With increasing off orientation the growth rate and layer thickness increase. Projected to a 2 inch epitaxial process local thickness variations of  $\pm 10\%$  have to be considered. The data in Figure 9 and Table 1 also include

polytype variations. However, the effect of grain polytype on FSGP growth rate is covered by the dominating grain orientation effect. It is estimated from the data in Table 1 that the variation of grain polytype impacts layer thickness is below 5%. Depending on the vapor pressure during FSGP the local influence is believed to be lowered in case of greater inert gas pressures [9].

## 3 Single-crystalline fluorescent SiC epitaxial growth

### 3.1 Homoepitaxial growth aspects of SiC

Historically, most studies of SiC epitaxial layers have been using the chemical vapor deposition (CVD) method. Initially, heteroepitaxial growth was performed on silicon substrates, and epitaxial layers of 3C-SiC were studied. In the 1990's, 6H-SiC substrates became commercially available from PVT growth, and allowed more intense homoepitaxial growth studies. The first wafers had an on-axis orientation, and this caused a competition between the homoepitaxial 6H-SiC growth and 3C-SiC inclusions. In order to reduce these inclusions, the surface was prepared with a slight off-axis orientation and the homoepitaxial growth could be fully realized without inclusions of other polytypes. The standard off-axis angle for the 6H-SiC became  $3.5^\circ$  in the [1120] direction. Later on, 4H-SiC substrates became available from the bulk growth. It was found that a  $3.5^\circ$  off-orientation was not sufficient to maintain the polytype stability in 4H-SiC, and inclusions of 3C-SiC appeared in the epitaxial growth. The standard off-orientation was modified to have an  $8^\circ$  off-axis for homoepitaxial growth in 4H-SiC.

In growth of nitride layers, the on-axis surface has been preferred. An off-axis surface could result in compositional

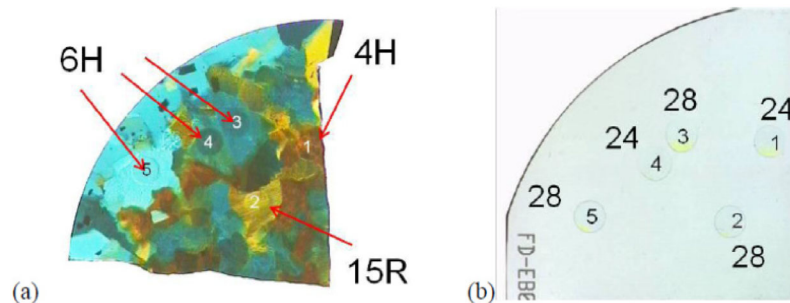


**Fig. 8.** Optical image of (a) poly-SiC source material and (b) grown 6H-SiC FSGP layer. The circles with numbers 1 to 5 indicate 5 growth areas selected by graphite mask.

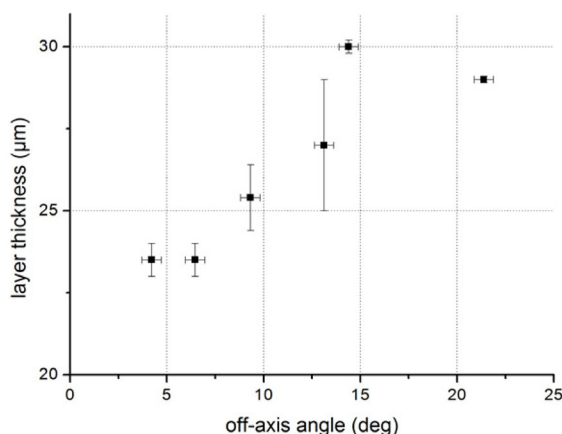


**Fig. 9.** Impact of off-axis angle orientation of poly-SiC source materials grains on growth rate/layer thickness during FSGP epitaxy (figure after Ref. [7]).

changes of the nitride layers, and a large off-axis is therefore very challenging to use. In the growth of fluorescent SiC homoepitaxial layers, the low off-axis growth was implemented [10–20]. This off-axis was in the range from  $0.8^\circ$  to  $1.4^\circ$ . Both SiC and nitride growth may then be adapted to handle polytype inclusions and compositional effects with some modifications of growth conditions.

For the fluorescent SiC layer, a voluminous layer is needed. The CVD method has shown to be promising for pure layers suitable for transistor applications, while a high growth rate has been challenging, and thick layers are hard to produce. The growth rate may be some tens of  $\mu\text{m}/\text{h}$ , but typically less than  $10 \mu\text{m}/\text{h}$  to maintain a reasonable surface morphology. The natural habit for SiC is sublimation. The use of close spacing for growing epitaxial layers has been introduced and applied for GaAs, Ge, GaP, and CdS [11]. The sublimation sandwich configuration that was applied for SiC [12,13] is a process that may be applied for growth of thick layers. This method was further elaborated in several studies by Kyoto Institute of Technology and Linköping University [14–16]. A version was applied to the growth of f-SiC on low off-axis SiC [17]. In particular, the ability to demonstrate the combination of fast sublimation growth process and structural quality makes the methods suitable for growth of fluorescent SiC [18].

In comparison, boule growth is typically applied by PVT growth at high temperature like  $2300\text{--}2500^\circ\text{C}$ . The corresponding growth rates are several hundreds of micrometer per hour. The growth is controlled by an ambient pressure of argon or nitrogen in the  $5\text{--}50$  mbar range. The typical source to seed distance is  $5\text{--}30$  mm, and the source is a SiC powder. The Fast Sublimation Growth Process (FSGP) [18] is a modification of the PVT growth. The growth temperature is reduced to less than  $2000^\circ\text{C}$  and use of vacuum or low pressure at which the surface kinetics is determining the growth rates rather than diffusion of species in the ambient. By a shorter distance between source and substrate to about  $1$  mm, the growth is epitaxial while the high growth rate and possibility of growing thick layers is maintained. Typical growth rates and growth temperatures are  $50\text{--}300 \mu\text{m}/\text{h}$  at  $1750\text{--}1900^\circ\text{C}$ .

### 3.2 Polytype stability and luminescence in fluorescent SiC layers

In general, the growth on off-oriented SiC substrates proceeds via step-flow growth [19]. In this mode, steps are created when the SiC is heated and at the initial stage of growth. Atoms on the surface are diffusing to the kink site of the step, and the polytype of the substrate is reproduced since the crystal arrangement is unique at the kink. With increasing layer thickness, there are on-axis regions that are created. These in principle are of two types. The first one is at the edge of the substrate, where an on-axis region is created in the upstep direction when the layers become very thick. The second is given by the terraces of the steps. When steps merge and give rise to step-bunching [20,21], the steps are increasing with their step height, but also in the width of the step. On the terrace, the on-axis region becomes larger. At some point, the atoms do not have time to diffuse to the step edge, and may form a growth center on the terrace. This might form as a 3C-SiC structure. Moreover, we have found that in the fluorescent 6H-SiC grown on the  $1.4^\circ$  off-axis substrate, the transition region from 6H-SiC to the 3C-SiC part also shows the presence of a series of stacking faults by the low temperature photoluminescence (LTPL) and high resolution transmission electron microscopy studies [22]. These stacking faults can trap the photo-excited carriers and thus reduce the luminescence efficiency.

**Table 1.** Summary of grain orientation (off-axis angle) and polytype of the source material on layer thickness during FSGP epitaxy (table after Ref. [7]).

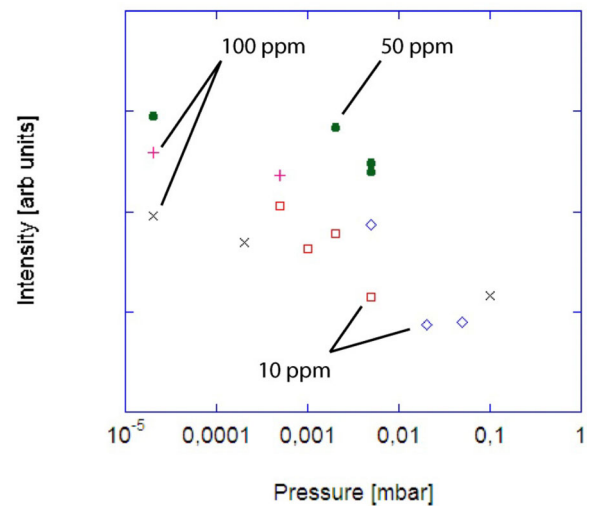
Grain	Polytype	Average layer thickness [ $\mu\text{m}$ ]	Off-orientation [deg]
1	4H	23.5	$4.2 \pm 0.5$
1	4H	23.5	$6.5 \pm 0.5$
2	15R	29	$21.4 \pm 0.5$
3	6H	27	$13.1 \pm 0.5$
4	6H	25.5	$9.3 \pm 0.5$
5	6H	30	$14.4 \pm 0.5$

**Fig. 10.** Surfaces of samples grown on quarter of 2 inch wafer with 50 ppm B doping: (a) overall figure, a 3C area is marked by a ring; (b) optical microscopy image, scale 10  $\mu\text{m}$ ; (c) SEM image, scale 4  $\mu\text{m}$ .

In general, the morphology of epitaxial layers grown by sublimation epitaxy shows a smooth surface without any traces of steps that can be observed in the optical microscope even when using Nomarski interference contrast mode, Figure 10. In comparison, the use of PVT source in growth of fluorescent silicon carbide layers gives rise to observable steps. In addition, the steps are quite straight in nominally undoped growth while some curvatures are observed in the doped growth. Typically in silicon carbide epitaxial and crystal growth, step bunching might appear when the C/Si ratio is high [23]. However, there is no graphitization of the PVT source that was used for the growth of the layers. In the sublimation epitaxy, if graphitization occurs, the source graphitizes first and then the epitaxial layer. The reason for faintly curved steps is not fully clear, but one could consider the influence of impurities on the step trains that gives rise to an instability. For example, it was observed that there is step bunching in PVT growth at high nitrogen concentration [24]. In that work, upon nitrogen doping, the regular step trains on 6H-SiC (0001) become unstable. The equidistant step trains are transformed into meandering macrosteps, explained by the nitrogen adsorption on the growing crystal surface.

The source material for a warm white LED contains only nitrogen and boron. This is produced by a mixture of boron carbide in the SiC source and having various nitrogen flows during the PVT growth. Thereby there will be both nitrogen and boron in the source. Boron is typically transferred at high ratio, around 80% is transferred from the poly-crystalline source to the growing epilayer. In comparison, nitrogen transfer is substantially less, like 10%.

In a simple PL set-up, one can distinguish the influence of high nitrogen content in the source. A series of PVT sources with different boron content in the SiC powder were grown at high nitrogen flow. The nitrogen seems

**Fig. 11.** Photoluminescence intensity change in a simple PL box with sources produced with 10, 50 and 100 ppm of boron at 8 sccm  $\text{N}_2$  flow at different initial levels of nitrogen ambient pressure.

to overcompensate the boron in all cases. However, the luminescence with different boron content is very scattered using an initial nitrogen pressure in the FSGP, shown in Figure 11. The initial ambient nitrogen pressure is set by closing of valves and there is a background ambient in contrast to the case when there is a constant flow of nitrogen. In the case when there is a high content of nitrogen in the source, the initial ambient nitrogen pressure is very low. Therefore, it is consequently also sensitive to changes in setting of initial pressure.

It seems that in source with high nitrogen content, there is no need to add nitrogen from the ambient. Therefore we have applied a static approach. In this, the system

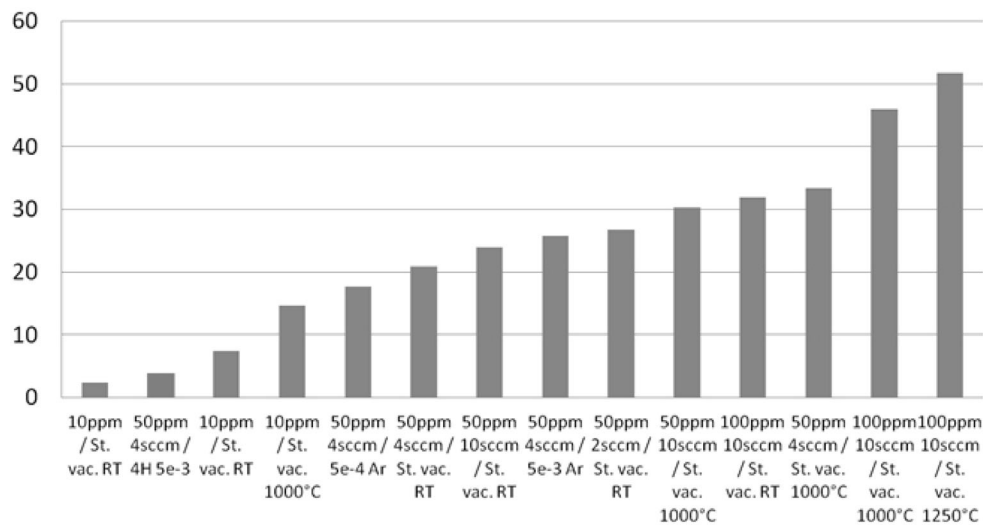


Fig. 12. Luminescence intensity with increasing boron doping and at which temperature the valve to pump is closed.

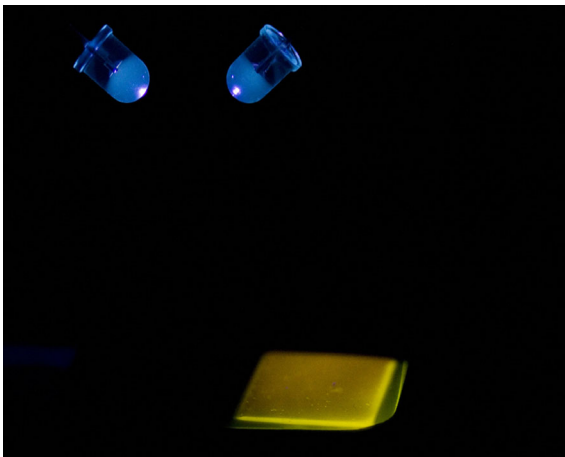


Fig. 13. N-B doped 6H-SiC that shows a luminescence even when excited by two weak ultraviolet LEDs.

is pumped to a base pressure around  $10^{-5}$  mbar. Then the valve is closed and heating starts. By this there is very low sensitivity to setting of ambient pressure since this is not operator dependent. We have applied three different conditions for such static vacuum approach. The valve to the pump was closed at three temperatures: room temperature (static RT), after heating to 1000 °C (static 1000), and heating to 1250 °C (static 1250). With this approach, the increase in luminescence with different concentrations of boron in the source, that has a high nitrogen content, shows a clear positive trend (Fig. 12).

Indeed, there is clear luminescence from the grown layers (Fig. 13). It has been shown that in sublimation epitaxy, there is a structural improvement from the substrate to the epilayer [25]. In FSGP growth of fluorescent layers, it was also observed that there is a perfect epitaxial relation between the substrate and the doped layers [10]. Thus, the FSGP is an attractive growth method to study fluorescent SiC due to the high quality material that the method produces.

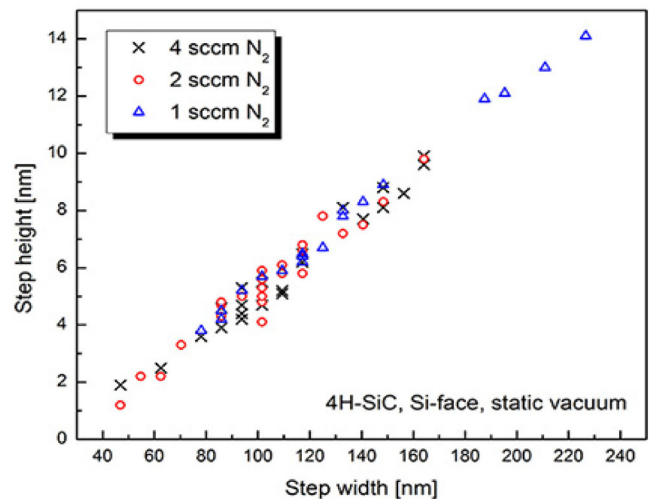
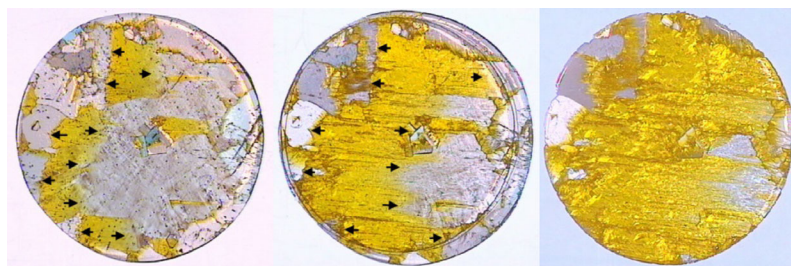


Fig. 14. Step width and step height in N-B doped 4H-SiC with source prepared with different nitrogen flows during PVT growth [26].

At lower doping of nitrogen during the PVT growth, the steps seem to be fairly similar as demonstrated in growth on  $4^\circ$  off-oriented 4H-SiC substrates (Fig. 14). There seems to be no pronounced influence on step-bunching or instabilities. It is likely that further increases in luminescence may be possible to obtain once the fundamental issues in growth and doping on the optical properties in fluorescent SiC are understood.

### 3.3 From inclusions to bulk: 3C-SiC and its photovoltaic potential

The sandwich configuration has many benefits. In particular, the high growth rate that is maintained as a benefit from the PVT growth mechanism is one interesting issue. This has shown that very thick layers may be produced.



**Fig. 15.** Three consecutive growths on one and the same wafer with diameter of 20 mm. The 3C-SiC region clearly expands with increasing layer thickness [27].

**Table 2.** Dopant concentrations and normalized PL peak intensities of the samples.

Sample	B concentration [cm <sup>-3</sup> ]	N concentration [cm <sup>-3</sup> ]	PL peak intensity [normalized to sample d]
a	$8.0 \times 10^{18}$	$4.0 \times 10^{16}$	0.0%
b	$6.9 \times 10^{18}$	$3.2 \times 10^{18}$	6.6%
c	$6.9 \times 10^{18}$	$6.0 \times 10^{18}$	8.3%
d	$4.4 \times 10^{18}$	$9.0 \times 10^{18}$	100%
e	$5.2 \times 10^{18}$	$9.2 \times 10^{18}$	77.1%

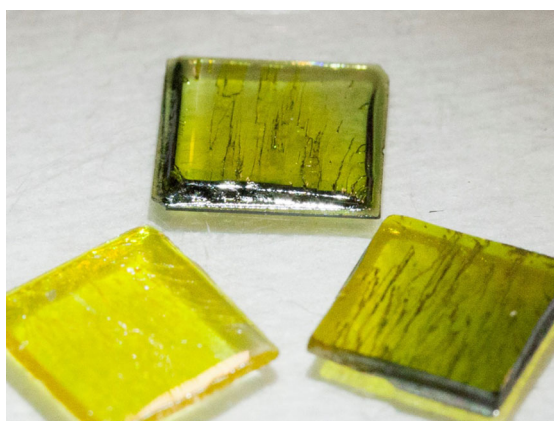


**Fig. 16.** Three free standing 3C-SiC substrates with size  $10 \times 10$  mm.

Also, the growth temperature is reduced compared with PVT. In fact, we have observed that 3C-SiC easily starts to nucleate. Figure 15 shows a repeated growth with initial 3C-SiC nucleation that expands upon further growth. Inclusions may appear also in the fluorescent silicon carbide layers, and it was shown that stacking faults appear in the 6H-SiC region close to the 3C-SiC [22]. The 3C-SiC inclusions, both in macroscopic and microscopic form, should be avoided since they will cause other radiation channels than in the donor to acceptor pair mechanism that is targeted.

In fact, by further growth and at higher growth rates, free standing and bulk-like 3C-SiC has shown to produce as high quality as 4H-SiC commercial substrates (Fig. 16) [28]. This is very interesting from an optoelectronic point of view. Cubic silicon carbide that is doped with boron fits very nicely in to the intermediate bandgap solar cell concept [29], which can be explored when the high quality material is possible to achieve.

## 4 Optical characterization of fluorescent SiC

With the application focus of SiC for light-emitting diodes, the FSGP grown 6H-SiC is characterized by using different technologies of photoluminescence and Raman spectroscopy in order to optimize its growth conditions for the wavelength conversion. A series of SiC samples (a–e) were grown with different B and N concentrations, and listed in Table 2. Details of the sample growth could be found in reference [30]. The concentration of the B and N are measured by using secondary ion mass spectroscopy (SIMS). For all the samples, the B concentration is in the order of  $10^{18}$  cm<sup>-3</sup>, while the N concentration increases dramatically from  $10^{16}$  to  $10^{18}$  cm<sup>-3</sup>.

### 4.1 Photoluminescence measurement [30]

The photoluminescence of the above 5 samples were measured by using an Olympus reflected fluorescence microscope system, a 377 nm diode laser as excitation source (focused by a 20× objective), and an instrument system CAS 140B spectrometer. The integration time was 10 s with excitation power density of 0.02 W/cm<sup>2</sup>, and the measurements were performed at room temperature.

As seen from Figure 17, the PL intensity increases as the N concentration increases from sample a, over b and c, to sample d. Then the intensity starts to decrease when the N concentration increases further from sample d to sample e. In general, the photoluminescence is quite weak for *p*-type doping samples a, b and c, so their spectra have to be enlarged in order to see any features. Samples d and e show very intensive yellow fluorescence, illustrated in Figure 17, compared to samples a, b, and c. According to the mechanism drawing in Figure 2, emission intensity increases as the dopants concentration increase, which is followed by samples a–d. The deviation from sample d to

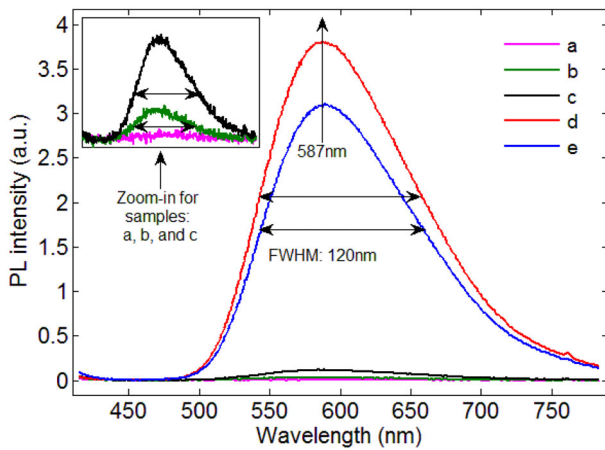


**Fig. 17.** Measured PL spectra of N-B co-doped 6H-SiC samples (inset: zoom-in for sample a, b, and c), same peak wavelength at 587 nm and full width at half maximum of 120 nm were observed in all the spectra.

sample e could be explained by the different ionization energy of donor and acceptor. For N and B, the concentration difference is of  $4.6 \times 10^{19} \text{ cm}^{-3}$  for the optimal sample.

#### 4.2 Raman spectroscopy [30]

Raman scattering spectra of the 6H-SiC samples were acquired in a backscattering configuration using the 514.5 nm line from an Ar ion laser (5 mW). The Raman spectra of the longitudinal optical phonon-plasmon coupled (LOPC) modes in the Raman spectra for 5 samples are shown in Figure 18, and the mechanisms of Raman shifts in *p*- and *n*-type samples are different. The LOPC mode would broaden, lower its intensity, and shift toward higher wavenumbers with increasing free carrier concentrations. Usually, it is more sensitive to the amount of free electrons than to free holes.

In *p*-type samples, very few acceptor states are ionized due to the large ionization energy, and the Raman shift is mainly contributed to the atomic size effect. The B atoms usually occupy Si lattice positions in SiC. The inter-atomic distance of a Si-C bond is longer than that of a B-C bond due to the smaller atomic radius of B. The biaxial tensile stress will be released which results in a decrease of the phonon oscillation frequency. So the LOPC mode shifts toward smaller wavenumbers with higher B concentrations.

For the *n*-type samples, the predominant mechanism causing the Raman shift of the LOPC mode is the free carrier (electron) concentration. Although no obvious peak shift has been observed between sample d and e due to the relatively small concentration difference, the peak intensity of the LOPC mode decreases as expected when the free electron concentration increases from sample e to d. Furthermore, one can see from Figure 18 that the LOPC modes of *n*-type samples occur at significantly higher wavenumbers than the *p*-type ones.

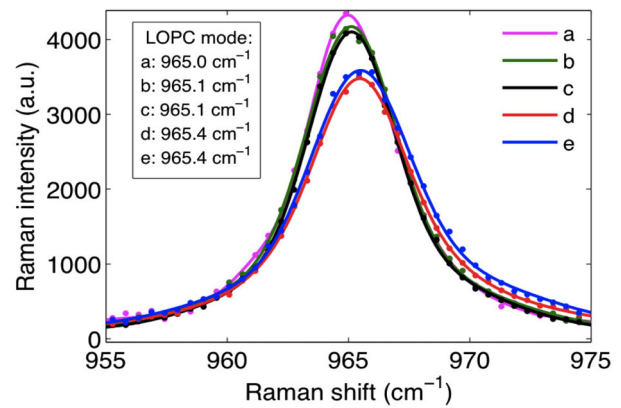


**Fig. 18.** LOPC mode in Raman spectra (inset: positions of LOPC modes of the SiC samples with different dopant concentrations).

#### 5 Light extraction enhancement for fluorescent SiC

Low extraction efficiency is a common problem for LED chips because the high refractive index of the semiconductor material confines most of the emitted light inside the device itself. It is challenging in the LED field to extract more light out of the device, therefore huge amount of effort has been made in the area to look for low-cost and effective solutions. Especially for fluorescent SiC based white LED, the SiC substrate has an even higher refractive index (2.65) than the sapphire substrate. Thus, it is a big issue to investigate. In this section, theoretical simulation is first made, in Section 5.1, as guidance for the later experiments. In order to implement the simulated structures, a couple of nanostructuring methods have been applied with the intention to achieve low cost and high scalability without sacrificing the efficiency, in Sections 5.2 to 5.5.

In the following sub-sections, the dry etching of SiC is done in a reactive ion etching (RIE) system (STS cluster system C010). The optimal etching conditions, i.e. the radio frequency (RF) power (100 W), process pressure (30 mT), and gas flow rates (24 sccm SF<sub>6</sub>, 6 sccm O<sub>2</sub>), are used, unless otherwise stated. Surface reflectance measurements of different SiC samples were carried out by using a goniometer system (Instrument Systems, GON360). A halogen lamp as a broadband light source was connected to the transmitter arm of the goniometer and the receiver arm was connected to an optical spectrometer (Instrument Systems, CAS140B). The SiC samples were mounted on the sample stage and the reflection spectra were measured with an incidence angle of 8° with respect to the surface-normal direction.

Angle-resolved photoluminescence measurements were carried out by using the same goniometer. A 377 nm diode laser was connected to the transmitter arm as the excitation light source and the SiC sample was optically excited from its back side at room temperature. The detection angle of the receiver arm was varied from 0° (surface-normal direction) to 85° with a step of 10° and the corresponding photoluminescence spectra were then acquired.

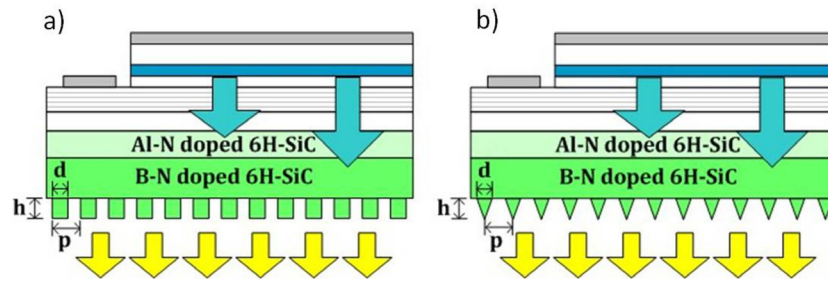


Fig. 19. Schematic cross-section of modeled SiC-based white LED (a) with cylinder structures, (b) with moth-eye structures.

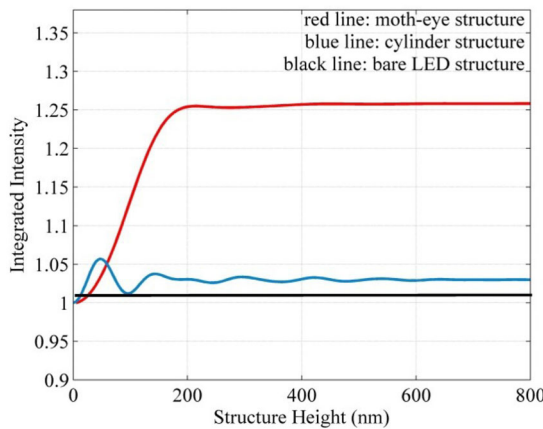


Fig. 20. Integrated intensity of cylinder (blue line) and moth-eye structures (red line) as functions of the structure height.

### 5.1 Simulation [31]

The simulation is based on the two dimensional rigid coupled-wave analysis (2D-RCWA) algorithm, and both moth-eye and cylinder structures are arranged in the hexagonal grid.

In both structures, the grating period is defined as  $p$  and is the distance between the centers of the neighboring structures,  $d$  is the width of the structure, and  $h$  is the height of the structure (illustrated in Figs. 19a and 19b). Since the structure width has very weak influence on the light transmittance, fixed values of  $d = 120$  nm and  $p = 1.4d$  have been applied as the optimized profile in all the following simulations. The working wavelengths were set to the whole visible light range from 360 to 800 nm. Normal light incidence to the surface was applied for the simplification. The structure height was varied from 0 to 800 nm in steps of 5 nm.

All the calculated results are normalized to the one without any structure applied. It is obviously shown in Figure 20 that moth-eye structure could improve the light extraction efficiency as high as 25%, which is much larger than the typical value of cylinder structure (2–3%). In order to reach as high as 25% extraction efficiency, the height of the cone structure should be larger than 180 nm, when the bottom diameter of the cone is 120 nm and the period of the cone is 168 nm.

From the simulation, the nanocone structures are much better than the nanocylinder structures in term

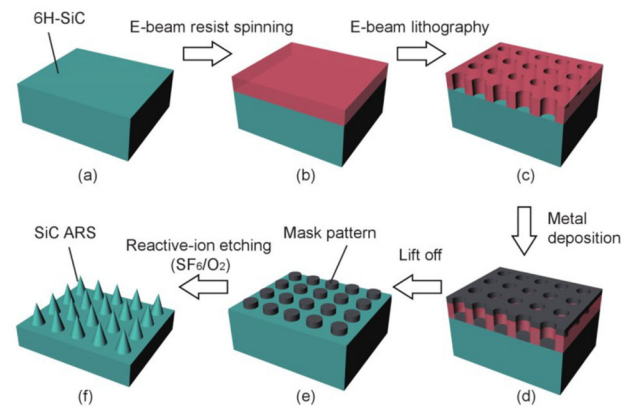


Fig. 21. Schematic illustrations of the SiC ARS fabrication process steps (a–f).

of enhanced transmittance. With this guidance, we have demonstrated experimentally the huge reflectance suppression and extraction efficiency enhancement in the following sections.

### 5.2 Periodic nanostructures made by e-beam lithography [32]

The periodic nanoconic anti-reflectance structures (ARS) are fabricated by using electron-beam lithography: firstly, the positive e-beam resist (ZEP520) was spin-coated on the SiC sample (Fig. 21a) and then pre-baked on a hot plate at 160 °C for 2 min (Fig. 21b). By using the e-beam writer (JEOL JBX9300FS) with a subsequent development process, the designed pattern was transferred to the e-beam resist coating (Fig. 21c). A hard mask material (chromium) layer was then deposited on the patterned SiC by the e-beam evaporation (Fig. 21d). Followed by a lift-off process, the dot-shaped pattern of chromium was obtained as a hard mask layer (Fig. 21e). The dry etching process using  $SF_6$  and  $O_2$  precursor gasses was carried out in the RIE system. After 12 min etching, the cone-shaped ARS with designed configuration (bottom diameter of 240 nm, pitch of 340 nm, height of 1.2  $\mu m$ , and hexagonal arrangement) were finally formed on the SiC surface (Fig. 21f).

The surface with nanostructures exhibits a highly suppressed average reflection from 21.6% for bare surface to

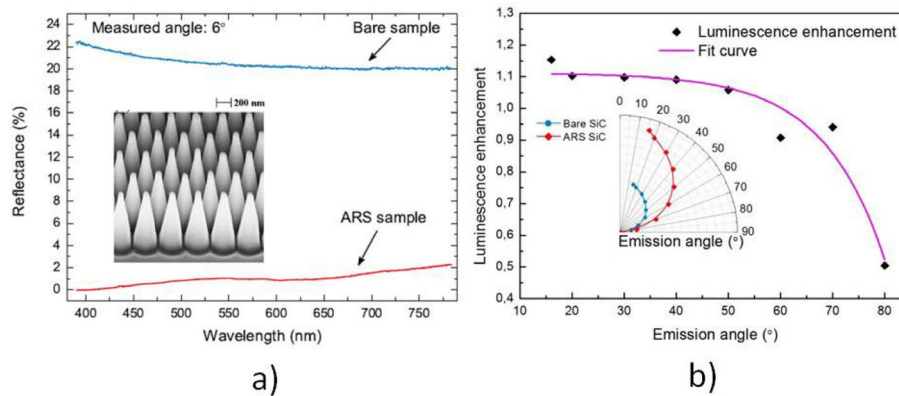


**Fig. 22.** (a) Surface reflectance (inset: SEM image of fabricated ARS on SiC) and (b) spatial emission pattern.

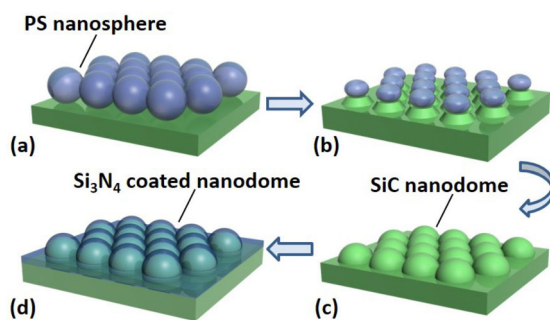


**Fig. 23.** Schematic diagram showing the detailed fabrication process of  $\text{Si}_3\text{N}_4$  coated nanodome structures on fluorescent SiC samples. (a) Formation of self-assembled polystyrene monolayer nanospheres as etching template, (b) dry etching process by RIE with  $\text{SF}_6$  and  $\text{O}_2$  gases, (c) formation of the nanodome structures on fluorescent SiC samples and, (d)  $\text{Si}_3\text{N}_4$  film deposition on SiC nanodome by PECVD.

1.6% for nanostructured sample (Fig. 22a). The light emission enhancement is omni-directional and the enhancement is larger than 100% for emission angle smaller than  $50^\circ$  (Fig. 22b).

### 5.3 Periodic nanostructures made by nanosphere lithography [33]

E-beam lithography is a slow, expensive and serial process, thus not suitable for mass-production. A potentially cost effective method, i.e. nanosphere lithography, is therefore investigated. The processing flow of the nanodome structures is shown schematically in Figure 23 and their corresponding SEM images are shown in Figure 24, respectively. Firstly, a monolayer hexagonal-close-packed array of polystyrene (PS) nanospheres with a diameter of 600 nm (size dispersion of 1%) was formed on a pre-treated SiC sample surface by a self-assembly method (see Fig. 23a). Subsequently, the SiC sample was subjected to RIE for pattern transfer, where the PS nanospheres monolayer serves as an etching template (see Fig. 23b). The PS nanospheres are a unique template as they shrink during the etching. After 5 min etching, the nanospheres are consumed completely and SiC nanodome (ND) structures are

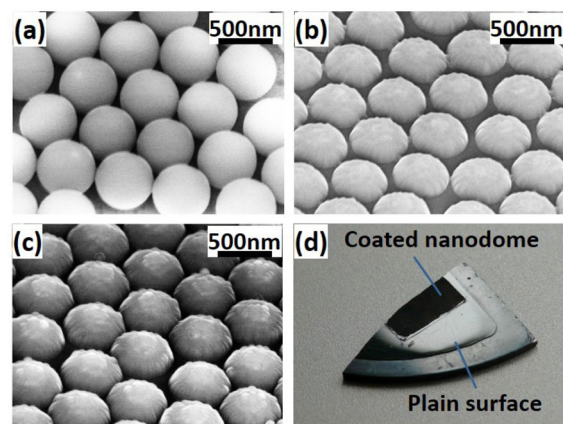


**Fig. 24.** Oblique-view SEM images of the (a) monolayer hexagonal-close-packed polystyrene nanospheres, (b) fabricated SiC nanodome structures, and (c)  $\text{Si}_3\text{N}_4$  coated nanodome structures, respectively. (d) A photograph of SiC sample with a partially plain surface (lower right part) and partially covered by the coated nanodome structures (upper left part).

achieved (see Fig. 23c). In addition, a 57 nm thick  $\text{Si}_3\text{N}_4$  coating with an intermediate refractive index ( $n = 2.0$ ) between the value of air ( $n = 1$ ) and 6H-SiC ( $n = 2.65$ ) was deposited on top of the nanodome structures by plasma-enhanced chemical vapor deposition (PECVD, STS cluster system C010). The  $\text{Si}_3\text{N}_4$  coated nanodome (CND) structures further enhance the extraction efficiency just for the proof-of-concept, although the optimal refractive index and the thickness for this purpose should be 1.64 and 72.5 nm, respectively. This cost-effective method has been approved to work by the surface reflectance measurement and photoluminescence measurement, shown in Figure 25.

The measured reflectance spectra in a wavelength range of 390–785 nm are shown in Figure 25a. The average reflectance of plain-SiC is around 20.5%. Due to the graded refractive index profile of nanodomed (ND) SiC, the average reflectance is significantly suppressed to 2.0%. An even lower average reflectance of 0.99% is obtained for the coated nanodomed (CND) SiC sample. Figure 25b shows that the fluorescent SiC sample exhibits

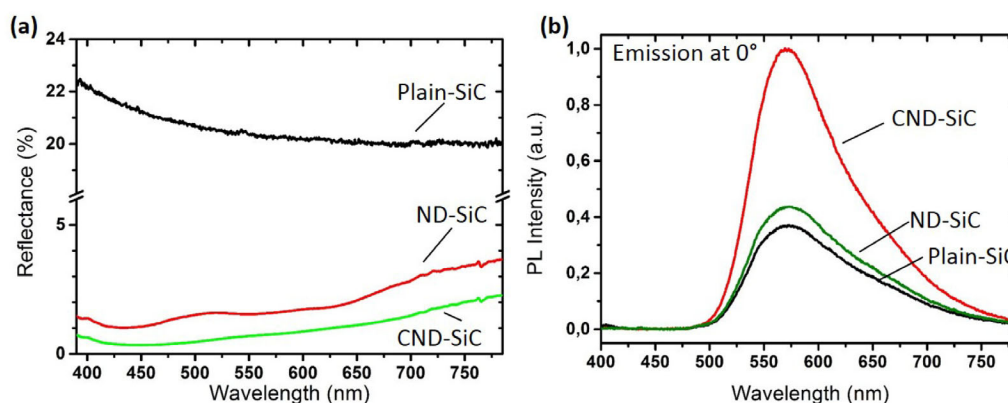


**Fig. 25.** (a) Surface reflectance suppression after the nanodome structuring and (b) light extraction enhancement after the nanodome structuring.

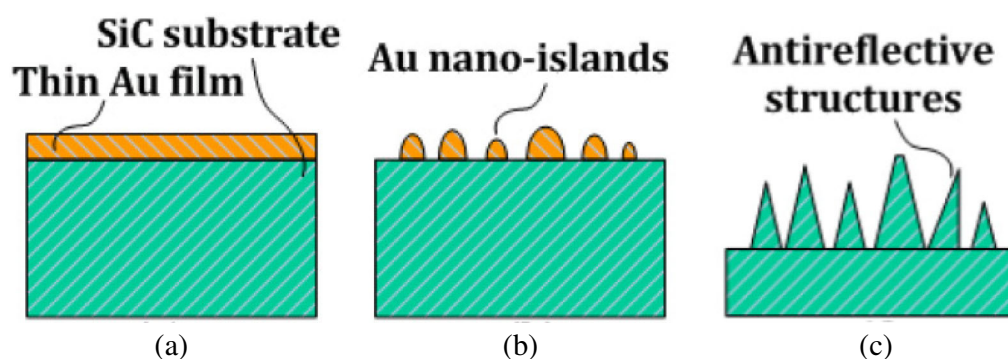


**Fig. 26.** Schematic illustrations of the SiC ARS fabrication process steps: (a) Au deposition; (b) thermal treatment of Au thin films to form nano islands; (c) RIE etch to form the nanocones by using Au nano islands as mask.

a broad luminescence peaked at 575 nm and the luminescence is enhanced after surface nanostructuring. Compared to plain-SiC, the ND-SiC demonstrates a 107% luminescence enhancement. Meanwhile, the luminescence of the CND-SiC is enhanced significantly by 138%. The observed photoluminescence enhancement results are in a good consistency with the experimental observations from the surface reflectance suppression measurements.

#### 5.4 Random nanostructures made by self-assembled metal nanoparticles [34,35]

Nanosphere lithography is not a standard LED fabrication process step. So it is difficult for this method to be adopted by the LED manufacturers. Therefore in addition to low cost and scalability, the new method should easily fit the current LED production line. Bearing this in mind, we developed a new method, i.e. using the self-assembled Au nano islands. The processing flow of this method is shown in Figure 26, (a) 10 nm Au film was deposited on the surface of SiC by e-beam evaporation; (b) the sample was then heat treated in N<sub>2</sub> for 5 min at 350 °C and nano-islands were formed; (c) the sample was then etched by RIE using CF<sub>4</sub> and O<sub>2</sub> and nanocone structures were formed. One oblique-view SEM image of the formed nanocone structures is shown in Figure 27a.

Their reflectance and photoluminescence are shown in Figures 27b and 27c, respectively, with comparison to bare samples.

Figures 27b and 27c show that the random nanostructures in this method are as good as the periodic ARS fabricated by e-beam lithography and nanosphere lithography. The reflectance is decreased to 1.6%, and the PL emission is enhanced by 67%.

#### 5.5 Random nanostructures made by thin Al film [36]

The random nanostructures made by the self-assembled Au have demonstrated light extraction enhancement at the same level as the periodic structures, although with relatively simpler process and better scalability. However, the usage of Au in mass production is still not a cheap enough solution. Therefore, a new low-cost method is developed, which uses thin aluminium (Al) film as the etching mask to form nanostructures and could easily fit to the current LED production line.

The processing steps to fabricate the nanostructures consist of a 60 nm Al thin film deposition (Alcatel) and reactive ion etching as shown in Figure 28. The processing details could be found from [36].

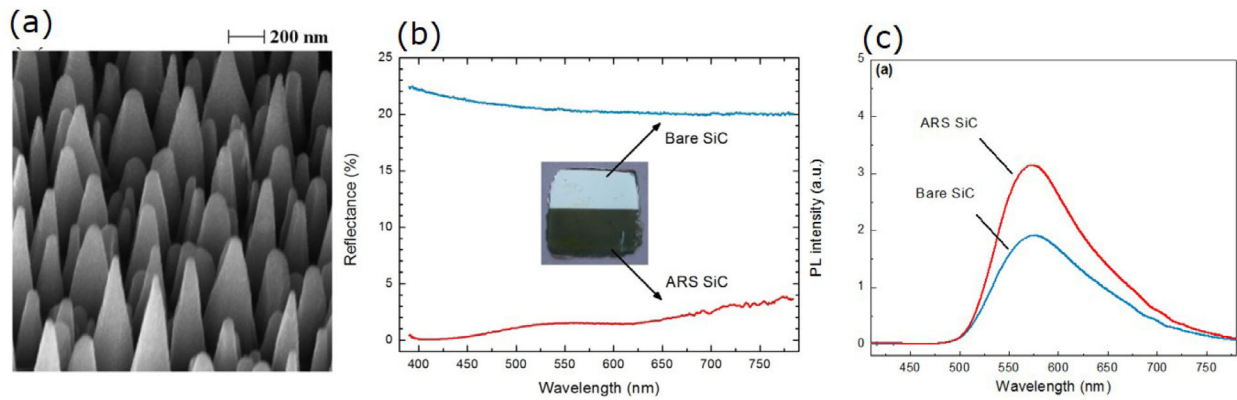


**Fig. 27.** (a) SEM image of the random nanocone structures, (b) surface reflectance in the visible light range for both bare samples and ARS SiC. The inset is an optical microscope image of a sample, half surface turned black after the nanostructuring, (c) photoluminescence enhancement of ARS sample, compared to bare SiC sample.



**Fig. 28.** Two-step processing to fabricate nanostructures using Al thin films: (1) Al deposition and (2) reactive ion etching.

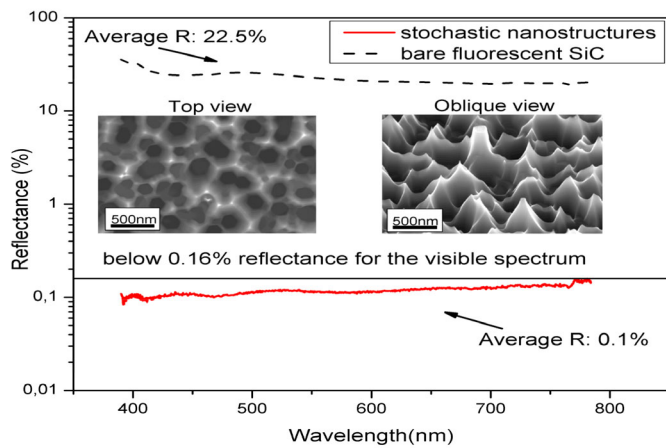


**Fig. 29.** Reflectance comparison between bare sample and nano-structured sample. The insets are SEM images of the f-SiC nanostructures (top view and oblique view).

Reflectance and photoluminescence measurements were performed on the nanostructured and bare f-SiC samples. The results for the reflectance of both bare sample and nanostructured sample are shown in Figure 29. The insets are SEM images of the top-view and oblique view nanostructures. The reflectance has been dramatically suppressed from 22.5% for bare sample to 0.1% for the nanostructured sample.

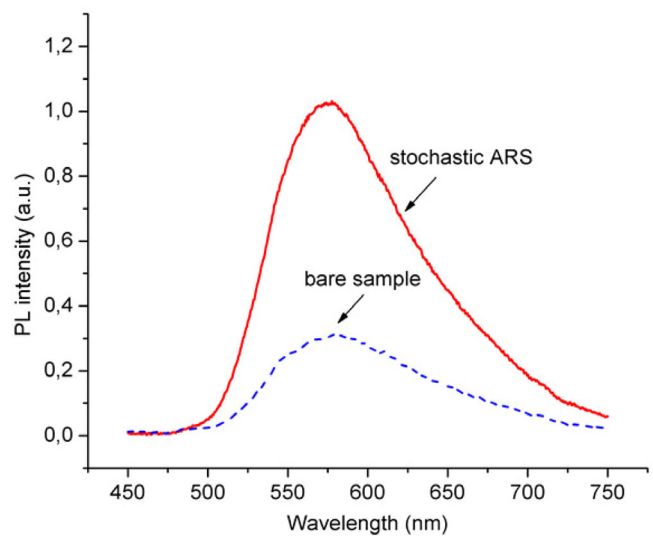


**Fig. 30.** Photoluminescence comparison between bare f-SiC sample and nanostructured f-SiC sample.

As shown in Figure 30, the photoluminescence of the sample with stochastic antireflection structures is enhanced by 210%, compared to that of the bare sample.

## 6 Conclusions and perspectives

Apart from the many advantages SiC brings in the electronic devices, it is also emerging as a promising material for optoelectronic devices. In this paper we have reviewed the poly-crystalline doped SiC growth by PVT method, the single-crystalline fluorescent SiC epitaxial growth by FSGP, as well as 4 different nanostructuring methods to enhance the extraction efficiency for the fluorescent SiC based white LEDs. The N-B codoped 6H-SiC has been demonstrated to be an ideal wavelength convertor thanks to its good crystal-quality and high wavelength conversion efficiency.

Four different methods (periodic nanostructures by e-beam lithography and nanosphere lithography, random nanostructures by self-assembled Au nanoparticles and thin Al film) have been developed to enhance the extraction efficiency and substantial emission intensity increase has been demonstrated for all these different nanostructuring methods. It is expected that further improvement could be achieved when the surface passivation is investigated. These nanostructuring methods in one hand could enhance the light extraction efficiency for LEDs, and in the other hand could also increase the energy efficiency for solar cells.

Despite using SiC as a wavelength converter for white LED, high crystal quality SiC LED is also proposed to be a prospective room temperature source for single photons, a critical device for quantum telecommunication and information processing [37].

In addition to the application in LEDs, 3C-SiC doped with B solar cell has been verified by simulation that its energy efficiency could reach as high as 48%, much higher than the 31% efficiency limit for single-junction Si solar cell. This so-called impurity photovoltaic effect has been proposed by Wolf since 1960 [38]. However, little experimental validation has been reported due to the poor crystal quality. As stated in Sections 2 and 3, we have now established a solid platform for the growth of crystalline SiC, and we hope to demonstrate this new concept experimentally.

Financial support by the Danish councils for strategic research funding (No. 09-072118), Proof of Concept funding, Danish Ministry of Science, Innovation and Higher Education, Swedish energy agency, Nordic energy research, Swedish research council (No. 2009-5307), Ångpanneföreningen Research Foundation, Richerts Foundation, STAEDTLER Foundation (Contract SH/eh 17/12) and BMBF (Contract INNER 03SG0393) are gratefully acknowledged.

## References

1. S. Kamiyama, T. Maeda, Y. Nakamura, M. Iwaya, H. Amano, I. Akasaki, H. Kinoshita, T. Furusho, M. Yoshimoto, T. Kimoto, J. Suda, A. Henry, I.G. Ivanov, J.P. Bergman, B. Monemar, T. Onuma, S.F. Chichibu, *J. Appl. Phys.* **99**, 093108 (2006)
2. P.T.B. Shaffer, *Appl. Opt.* **10**, 1034 (1971)
3. V. Jokubavicius, P. Hens, R. Liljedahl, J.W. Sun, M. Kaiser, P. Wellmann, S. Sano, R. Yakimova, S. Kamiyama, M. Syväjärvi, *Thin Solid Films* **522**, 7 (2012)
4. X. Bourrat, B. Trouvat, G. Limousin, G. Vignoles, F. Doux, *J. Mater. Res.* **15**, 92 (2000)
5. T.L. Straubinger, M. Bickermann, R. Weingärtner, P.J. Wellmann, A. Winnacker, *J. Cryst. Growth* **240**, 117 (2002)
6. P. Wellmann, P. Desperrier, R. Müller, T. Straubinger, A. Winnacker, F. Baillet, E. Blanquet, J.M. Dedulle, M. Pons, *J. Cryst. Growth* **275**, e555 (2005)
7. M. Kaiser, T. Hupfer, V. Jokubavicius, S. Schimmel, M. Syväjärvi, Y. Ou, H. Ou, M.K. Linnarsson, P. Wellmann, *Mater. Sci. Forum* **740**, 39 (2013)
8. M. Kaiser, S. Schimmel, V. Jokubavicius, M.K. Linnarsson, H. Ou, M. Syväjärvi, P. Wellmann, *Nucleation and growth of polycrystalline SiC*, accepted by *Materials Science Engineering B*
9. T. Hupfer, P. Hens, M. Kaiser, V. Jokubavicius, M.L. Syväjärvi, P.J. Wellmann, *Mater. Sci. Forum*, **740**, 52 (2013)
10. M. Syväjärvi, J. Müller, S.W. Sun, V. Grivickas, Y. Ou, V. Okubavicius, P. Hens, M. Kaiser, K. Ariyawong, K. Gulbinas, P. Hens, R. Liljedahl, M.K. Linnarsson, S. Kamiyama, P. Wellmann, E. Spiecker, H. Ou, *Phys. Scr.* **T148**, 014002 (2012)
11. F.H. Nicoll, *J. Electrochem. Soc.* **110**, 1165 (1963)
12. Y.A. Vodakov, E.N. Mokhov, M.G. Ramm, A.D. Roenkov, *Kristall und Technik* **14**, 729 (1979)
13. E.N. Mokhov, I.L. Shulpina, A.S. Treguva, Yu.A. Vodakov, *Crystal Res. Tech.* **16**, 879 (1981)
14. T. Yoshida, Y. Nishio, S.K. Lilov, S. Nishino, *Mater. Sci. Forum* **264-268**, 155 (1998)
15. A. Kakanakova-Georgieva, M.F. MacMillan, S. Nishino, R. Yakimova, E. Janzén, *Mater. Sci. Forum* **264-268**, 147 (1998)
16. M. Syväjärvi, R. Yakimova, M.F. MacMillan, M. Tuominen, A. Kakanakova-Georgieva, C.G. Hemmingsson, I.G. Ivanov, E. Janzén, *Mater. Sci. Forum* **264-268**, 143 (1998)
17. Y. Kawai, T. Maeda, Y. Nakamura, Y. Sakurai, M. Iwaya, S. Kamiyama, H. Amano, I. Akasaki, M. Yoshimoto, T. Furusho, H. Kinoshita, H. Shiomi, *Mater. Sci. Forum* **527-529**, 263 (2006)
18. M. Syväjärvi, R. Yakimova, in *The Comprehensive Semiconductor Science & Technology (SEST)*, edited by P. Bhattacharya, R. Fornari, H. Kamimura (Elsevier, 2011), pp. 202–231
19. K. Shibahara, N. Kuroda, S. Nishino, H. Matsunami, *Jpn J. Appl. Phys.* **26**, L1815 (1987)
20. T. Kimoto, A. Itoh, H. Matsunami, *Appl. Phys. Lett.* **66**, 3645 (1995)
21. M. Syväjärvi, R. Yakimova, E. Janzén, *J. Cryst. Growth* **236**, 297 (2002)
22. J.W. Sun, T. Robert, A. Andreadou, A. Mantzari, V. Jokubavicius, R. Yakimova, J. Camassel, S. Juillaguet, E.K. Polychroniadis, M. Syväjärvi, *J. Appl. Phys.* **111**, 113527 (2012)
23. T. Kimoto, A. Itoh, H. Matsunami, T. Okano, *J. Appl. Phys.* **81**, 3494 (1997)
24. N. Ohtani, M. Katsuno, J. Takahashi, H. Yashiro, M. Kanaya, *Phys. Rev. B* **59**, 4592 (1999)
25. M. Syväjärvi, R. Yakimova, H. Jacobsson, E. Janzén, *J. Appl. Phys.* **88**, 1407 (2000)
26. S. Schimmel, M. Kaiser, P. Hens, V. Jokubavicius, R. Liljedahl, J. Sun, R. Yakimova, Y. Ou, H. Ou, M.K. Linnarsson, P.J. Wellmann, M. Syväjärvi, *Mater. Sci. Forum* **740-742**, 185 (2013)
27. M. Syväjärvi, R. Yakimova, H. Jacobsson, E. Janzén, *Mater. Sci. Forum* **353-356**, 143 (2001)
28. J.W. Sun, I.G. Ivanov, R. Liljedahl, R. Yakimova, M. Syväjärvi, *Appl. Phys. Lett.* **100**, 252101 (2012)
29. M. Syväjärvi, *Adv. Mater. Lett.* **3**, 175 (2012)
30. Y. Ou, V. Jokubavicius, S. Kamiyama, C. Liu, R.W. Berg, M. Linnarsson, R. Yakimova, M. Syväjärvi, H. Ou, *Opt. Mater. Express* **1**, 1439 (2011)

31. Y. Ou, D.D. Corell, C. Dam-Hansen, P.M. Petersen, H. Ou, *Opt. Express* **19**, A166 (2011)
32. Y. Ou, V. Jokubavicius, P. Hens, M. Kaiser, P. Wellmann, R. Yakimova, M. Syväjärvi, H. Ou, *Opt. Express* **20**, 7575 (2012)
33. Y. Ou, X. Zhu, U. Møller, S. Xiao, H. Ou, Broadband antireflection nanodome structures on SiC substrate, in *Group IV photonics, WP3, Soul, 2013*
34. Y. Ou, I. Aijaz, V. Jokubavicius, R. Yakimova, M. Syväjärvi, H. Ou, *Opt. Mater. Express* **3**, 86 (2013)
35. Y. Ou, V. Jokubavicius, R. Yakimova, M. Syväjärvi, H. Ou, *Opt. Lett.* **37**, 3816 (2012)
36. A. Argyraki, Y. Ou, H. Ou, *Opt. Mater. Express* **3**, 1119 (2013)
37. F. Fuchs, V.A. Soltamov, S. Vaeth, P.G. Baranov, E.N. Mokhov, G.V. Astakhov, V. Dyakonov, *Sci. Rep.* **3**, 1637 (2013)
38. M. Wolf, *Proceedings of the IRE* **48**, 1246 (1960)